Experimental and theoretical evidence for bilayer-by-bilayer surface melting of crystalline ice

Sánchez, Maria Alejandra; Kling, Tanja; Ishiyama, Tatsuya; van Zadel, Marc-Jan; Bisson, Patrick J.; Mezger, Markus; Jochum, Mara N.; Cyran, Jenee D.; Smit, Wilbert J.; Bakker, Huib J.; Shultz, Mary Jane; Morita, Akihiro; Donadio, Davide; Nagata, Yuki; Bonn, Mischa; Backus, Ellen H. G.

Published in:
Proceedings of the National Academy of Sciences of the United States of America

Link to article, DOI:
10.1073/pnas.1612893114

Publication date:
2017

Document Version
Publisher's PDF, also known as Version of record

Experimental and theoretical evidence for bilayer-by-bilayer surface melting of crystalline ice

M. Alejandra Sánchez[a], Tanja Kling[a], Tatsuya Ishiyama[b], Marc-Jan van Zadel[a], Patrick J. Bisson[c], Markus Mezger[a,d], Mara N. Jochum[a,e], Jenée D. Cyran[a], Wilbert J. Smit[f], Huib J. Bakker[f], Mary Jane Shultz[c], Akihiro Morita[g,h], Davide Donadio[a,i], Yuki Nagata[a], Mischa Bonn[a,1], and Ellen H. G. Backus[a,1]

[a]Max Planck Institute for Polymer Research, 55128 Mainz, Germany; [b]Graduate School of Science and Engineering, University of Toyama, Toyama 930-8555, Japan; [c]Laboratory for Water and Surface Studies, Department of Chemistry, Pearson Laboratory, Tufts University, Medford, MA 02155; [d]Institute of Physics, Johannes Gutenberg University Mainz, 55128 Mainz, Germany; [e]BASF SE, 67117 Limburgerhof, Germany; [f]FOM Institute AMOLF, 1098 XG Amsterdam, The Netherlands; [g]Department of Chemistry, Graduate School of Science, Tohoku University, Sendai 980-8578, Japan; [h]Elements Strategy Initiative for Catalysts and Batteries, Kyoto University, Kyoto 615-8520, Japan; and [i]Department of Chemistry, University of California, Davis, CA 95616

Edited by Daan Frenkel, University of Cambridge, Cambridge, United Kingdom, and approved November 15, 2016 (received for review August 4, 2016)

On the surface of water ice, a quasi-liquid layer (QLL) has been extensively reported at temperatures below its bulk melting point at 273 K. Approaching the bulk melting temperature from below, the thickness of the QLL is known to increase. To elucidate the precise temperature variation of the QLL, and its nature, we investigate the surface melting of hexagonal ice by combining noncontact, surface-specific vibrational sum frequency generation (SFG) spectroscopy and spectra calculated from molecular dynamics simulations. Using SFG, we probe the outermost water layers of distinct single crystalline ice faces at different temperatures. For the basal face, a stepwise, sudden weakening of the hydrogen-bonded structure of the outermost water layers occurs at 257 K. The spectral calculations from the molecular dynamics simulations reproduce the experimental findings; this allows us to interpret our experimental findings in terms of a stepwise change from one to two molten bilayers at the transition temperature.

crystalline ice | surface melting | sum frequency generation | stepwise | water

As early as 1859, Faraday proposed the existence of a liquid-like layer at ice surfaces (1, 2). This surface-induced ice melting represents one of the most prominent examples of an interface-induced premelting phase transition (3, 4). During the last decades, the so-called quasi-liquid layer (QLL) at the ice–air interface, wetting the crystalline bulk phase, has been studied by theory (5), computer simulations (6–8) and various experimental techniques (9–17). Despite the general agreement on the presence of a QLL below the bulk freezing point, the temperature-dependent thickness of the QLL has remained controversial. The experimentally reported onset temperature for QLL formation varies between 200 K and 271 K. Moreover, most experimental work shows that, with increasing temperature, the QLL thickness gradually and continuously increases from the onset temperature up to the bulk melting point, with reported thicknesses varying from 2 nm to over 45 nm at 271 K (3, 11–13, 15, 16, 18). In contrast, early simulations showed that the QLL is formed in a more quantized, bilayer-by-bilayer manner (8).

We provide evidence of layer-by-layer growth of the QLL at the ice–air interface by combining experiments with simulations. We use surface-specific vibrational sum-frequency generation (SFG) spectroscopy. Our experimental data are corroborated by spectral calculations based on molecular dynamics (MD) simulations. SFG spectra provide unique information on the vibrational response of the outermost molecules of a centrosymmetric solid, such as the proton-disordered ice studied here. At the interface, the symmetry is broken, thus allowing us to specifically probe the vibrational response of the interfacial region. The signal is strongly enhanced when the infrared laser pulse is resonant with a molecular vibration (19). The amplitude of the signal depends on the number of vibrational chromophores and its transition dipole moment, the amount of order present at the interface, and intramolecular/intermolecular coupling effects.

Therefore, SFG spectroscopy has been used for unveiling the molecular conformation of the ice–air interface. Shen and coworkers (20, 21) focused on the frequency region of the nonhydrogen-bonded OH stretch mode (3,600 cm^{-1} to 3,800 cm^{-1}) in the temperature range from 173 K to 271 K. By probing these OH groups, which stick into the air, they concluded that surface disordering appears at temperatures as low as 200 K. The Shultz group (22–25) studied the hydrogen-bonded OH stretch frequency region (3,200 cm^{-1} to 3,600 cm^{-1}) of various basal and prism faces of the ice–air interface at temperatures around 100 K.

To study surface melting, we focus here on the hydrogen-bonded part of the spectrum between 235 K and 273 K where, according to most reports (18), surface melting takes place. As the frequency of the OH stretch vibration depends on the hydrogen bond strength with neighboring molecules (26, 27), the SFG spectrum contains information on the intermolecular interactions between water molecules at the surface; this allows us to determine the hydrogen bond strength at the interface and to obtain information about the QLL.

In this study, we explore mainly the surface melting of the basal plane of hexagonal ice (ice Ih), which is the most common ice phase. In ice Ih, the oxygen atoms are located in the wurtzite structure. The hydrogen atoms are arranged according to the

Significance

Over 150 years ago, Faraday discovered the presence of a water layer on ice below the bulk melting temperature. This layer is important for surface chemistry and glacier sliding close to subfreezing conditions. The nature and thickness of this quasi-liquid layer has remained controversial. By combining experimental and simulated surface-specific vibrational spectroscopy, the thickness of this quasi-liquid layer is shown to change in a noncontinuous, stepwise fashion around 257 K. Below this temperature, the first bilayer is already molten; the second bilayer melts at this transition temperature. The blue shift in the vibrational response of the outermost water molecules accompanying the transition reveals a weakening of the hydrogen bond network upon an increase of the water layer thickness.

Author contributions: D.D., M.B., and E.H.G.B. designed research; M.A.S., T.K., T.I., M.-J.v.Z., M.M., M.N.J., J.D.C., A.M., and Y.N. performed research; M.A.S., T.K., T.I., M.M., M.N.J., J.D.C., A.M., D.D., Y.N., and E.H.G.B. analyzed data; M.A.S., T.K., T.I., M.-J.v.Z., P.J.B., M.M., W.J.S., H.J.B., M.J.S., A.M., D.D., Y.N., M.B., and E.H.G.B. wrote the paper; P.J.B. and M.J.S. assisted in setting up the experiment; and W.J.S. and H.J.B. assisted in the analysis.

The authors declare no conflict of interest.

This article is a PNAS Direct Submission.

Freely available online through the PNAS open access option.

[1]To whom correspondence may be addressed. Email: backus@mpip-mainz.mpg.de or bonn@mpip-mainz.mpg.de.

This article contains supporting information online at www.pnas.org/lookup/suppl/doi:10.1073/pnas.1612893114/-/DCSupplemental.

Bernal–Fowler ice rules (28). Depending on the orientation of the ice crystal, different crystallographic planes are exposed to air. Top and side views of the basal plane (0001), a primary prism plane ($10\bar{1}0$), and a secondary prism plane ($\bar{1}2\bar{1}0$) are schematically shown in Fig. 1 and Table S1. In the direction perpendicular to the basal and primary prism planes, the oxygen atoms form a bilayer structure. In contrast, in the direction perpendicular to the secondary prism plane, oxygen layers are equidistant.

To obtain well-defined ice samples, single crystals were grown from a melt using the seed extraction method (29, 30) based on the Czochralski process (31) (Fig. S1). Cylindrical ice single crystals (60 mm diameter, 30 mm length) were obtained by slowly withdrawing the seed from the melt. Single crystallinity was checked using crossed polarizers in a Rigsby stage (32). Samples with different surface orientation were characterized by Formvar etching (Fig. S2) and X-ray diffraction (Fig. S3 and Table S2). Details on ice growth and characterization can be found in *Materials and Methods* and *Supporting Information*.

Results and Discussion

Fig. 2 displays the SFG spectra under *ssp* polarization (*s*, SFG; *s*, visible; *p*, IR) of the basal ice face at different temperatures. See *Materials and Methods* and Fig. S4 for details of the SFG experiments. An intense peak slightly below 3,200 cm^{-1} is observed, which agrees with the previous SFG measurements (21). As the temperature increases from 235 K to 264 K, the intensity decreases by a factor of 5. Similar trends are observed for the secondary prism face of ice (Fig. S5). Wei et al. (21) reported a similar, albeit much weaker, intensity decrease by a factor of 3 with increasing temperature from 173 K to 272 K. In contrast, a strong temperature dependence has been reported by the Shultz group. They observed an intensity decrease by approximately a factor of 6 in the temperature range from 113 K to 178 K (24). The decrease in the ice SFG intensity with increasing temperature has previously been interpreted as a decrease in the (bulk-allowed) quadrupole contribution (22, 33) and a loss in the tetrahedral hydrogen bond structure leading to a decrease in the intermolecular coupling (34, 35).

Besides the intensity variation [$I(\omega)$], Fig. 2*A* also shows an apparent shift of the hydrogen-bonded OH stretch band to higher-frequency (ω) with increasing temperature. To quantify the frequency shift as a function of temperature, the numerically determined first moment of the spectral distribution, $\int \omega I(\omega)d\omega / \int I(\omega)d\omega$, of the hydrogen-bonded OH peak has been plotted in Fig. 2*B*. Surprisingly, the first moment of the spectral distribution exhibits not a gradual shift with increasing temperature but rather a steep increase from ~3,185 cm^{-1} to ~3,210 cm^{-1} around 257 K. A sigmoidal fit gives the transition temperature at 256.9 ± 0.3 K (i.e., −16 °C). For the secondary prism face (*c* axis oriented perpendicular to plane of incidence), we also observe a decrease in intensity and a shift to higher frequency with increasing temperature (Fig. 2*B*), whereas the observed shift is smaller than that for the basal face. A sigmoidal fit results in a transition temperature at 258.6 ± 0.1 K (i.e., −14 °C). As a higher frequency of the OH stretch mode of water indicates a weakening of the hydrogen bonds' strengths (26, 27), the sigmoidal shape may be interpreted as an abrupt weakening of the hydrogen bonds in the top layers of the ice sample for both the basal and, although smaller, the secondary prism face.

Interestingly, the spectra between 235 K and 269 K can be very well described by a linear combination of the spectra at 235 and 269 K, where the higher temperature spectrum is blue shifted. The relative amplitudes of the 235 and 269 K spectra to the spectra at intermediate temperatures inferred from the fits (red curves in Fig. 2*A*) are plotted in Fig. 2*C*. Only the amplitude of the 235 and 269 K spectral contribution are free parameters. The contribution of the 235 K spectrum decreases linearly with increasing temperature, whereas the contribution of the 269 K spectrum has a stepwise increase from zero to a finite value around 254 K.

Besides the hydrogen-bonded OH stretch region, the vibrational response of OH bonds sticking out of the surface, i.e., dangling OHs, also contains potentially important information about the nature of the surface. The vibrational frequency of this mode is rather high, around 3,700 cm^{-1}, as the OH group does not form a hydrogen bond. Fig. 3*A* shows the SFG spectra in the frequency range from 3,630 cm^{-1} to 3,760 cm^{-1} for various temperatures that reveal a moderate, continuous reduction of the free OH intensity with increasing temperature. The peak amplitude can be obtained by calculating the peak area between 3,630 cm^{-1} and 3,760 cm^{-1}. As apparent from the data in Fig. 3*B*, the amplitude of the 3,700 cm^{-1} mode shows only a weak, continuous temperature dependence, indicating that the outermost surface structure does not change dramatically, in agreement with previous results by Shen and coworkers (20). The secondary prism face shows the same trend.

To connect the experimental results to a molecular-level picture, MD simulations were performed using the TIP4P/Ice model, showing the melting point at 272.2 K (36). The details of the simulation are given in *Materials and Methods* and *Supporting Information*. Fig. 4 and Fig. S6 show the density profiles for different temperatures for the basal and secondary prism faces. The double peaks for basal face and a single peak for prism face manifest the bilayer structure for the basal face and the single-layer structure for the secondary prism face, respectively. The observed density profiles resemble those reported in previous works (7, 8). At 230 K, the density profile for the slab cleaved

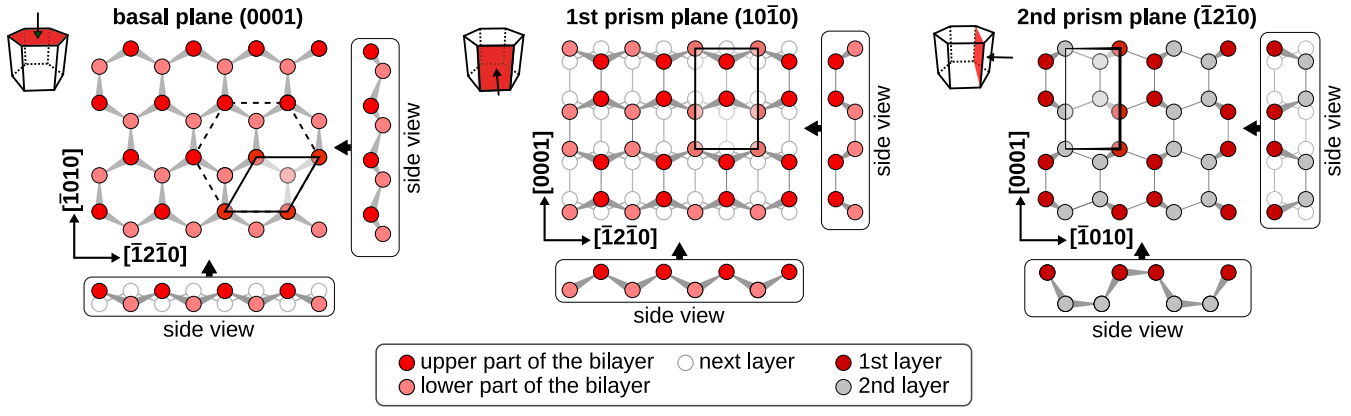

Fig. 1. High symmetry faces of ice Ih. Top view of the basal (*Left*), primary prism (*Center*), and secondary prism (*Right*) face of ice Ih. Circles represent oxygen atoms. The crystallographic unit cell is highlighted by solid black lines. Dashed lines and *Insets* indicate the hexagonal symmetry. For the basal and primary prism plane, dark and light red circles represent oxygen atoms in the upper and lower part, respectively, of the bilayer. For the secondary prism plane, the first (dark red) and second (gray) layers are shown. Shaded circles indicate the positions of oxygen atoms in underlying layers. At the surface, each "upper molecule" (either upper part of the bilayer or of the first layer) contributes exactly one dangling OH bond.

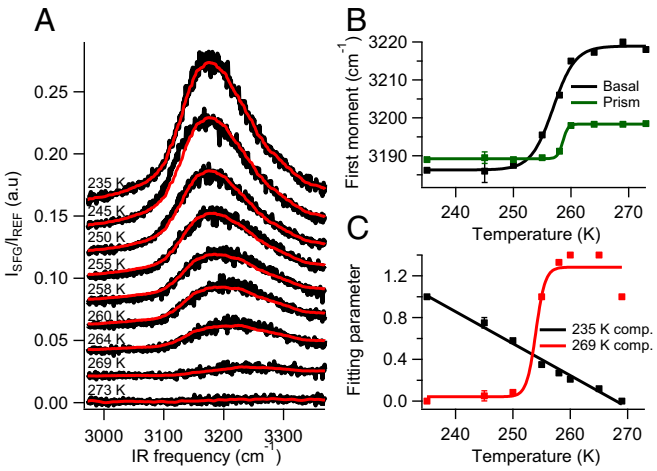

Fig. 2. Ice–quasi-liquid–air interface studied with SFG. (*A*) SFG spectra under *ssp* polarization between 235 K and 273 K for the basal face of ice Ih. The black lines are the experimental results; the red lines are results of the two component fit (see *Results and Discussion*). The data are offset for clarity. (*B*) First moment of the spectral intensities shown at different temperatures for the basal and secondary prism face averaged over up to four different experiments. The lines are sigmoidal fits through the data points. (*C*) Contribution of the 235 K and 269 K spectra to the SFG spectra at intermediate temperatures, for the basal face. Typical error bars based on reproducibility from experiment to experiment are given in the graph.

along the basal plane displays a double peak structure for all bilayers, except the outermost bilayer, indicating that the outermost layer is already disordered at this temperature. This trend is also supported by the radial distribution function (RDF), which, for the outer layer, is similar to the water reference, whereas it retains the structure of ice from the second layer inward (Fig. S7). The double peak fine structure in the second layer suddenly disappears between 260 K and 270 K. At the same temperature, the RDF for the second layer loses crystalline features and turns liquid-like. Moreover, the exchange of water molecules between the layers increases around this temperature. The orange lines in Fig. 4 and Fig. S7 mark the molten layers based on the absence of the double peak structure in the density profile and the liquid features of the RDF. These two parameters indicate that the basal plane melts in a bilayer-by-bilayer fashion, in agreement with the findings of Kroes (8). The density profiles of the slab exposing the secondary prism face show that melting occurs gradually, as the difference between density peaks and valleys in the surface layers decreases progressively.

Subsequently, SFG spectra are calculated to connect the molecular-level changes to the spectrum. The modeling details can be found in *Materials and Methods* and in *Supporting Information*. Fig. 5*A* shows the calculated *ssp* polarized SFG intensity spectra of the basal face of ice as a function of temperature in the hydrogen-bonded and the dangling OH regions of the spectrum. In the simulations, only the first two outer bilayers were taken into account. The inner bilayers were assumed not to contribute to the SFG signal, because they have inversion symmetry, which can be seen from the orientation of the O–H group plotted in Fig. 6. At low temperature (Fig. 6*A*), the distribution is symmetric ("up" and "down") for the third bilayer, whereas the first two layers show asymmetry resulting in an SFG signal. At 230 K, the hydrogen-bonding stretching band has a relatively intense peak in the SFG spectrum near 3,200 cm^{-1}. Similar to the experiments, with increasing temperature, the peak intensity decreases and the peak maximum appears to shift toward higher frequencies. As evident from Fig. 5*B*, a sigmoidal fit through the peak maximum of hydrogen-bonded OH stretch mode as a function of temperature results in an inflection point at 252 ± 1 K (i.e., −21 °C). This temperature is slightly lower than the temperature observed in the density profiles reported in Fig. 4. However, these simulations were performed using a different force field (see *Supporting Information* for details). Also in agreement with the experiments, the dangling OH band at about 3,700 cm^{-1} shows a moderate reduction with increasing temperature (Fig. 5*C*).

A more detailed look into the orientation of the water molecules provides more details on the molecular origin of the temperature-dependent change in the calculated SFG signal. Fig. 6*C* shows the two maxima for the probability distributions of up- and down-oriented O–H groups of the water molecules of the second bilayer. Clearly, the probability maximum decreases with increasing temperature as the water becomes more disordered, making the distribution wider and the maximum consequently lower. However, this change is not continuous: between 250 K and 260 K, the slope of the curves in Fig. 6*C* alters, reflecting a larger change of the disorder of the orientation of the water molecules for a given temperature step, apparently caused by melting of the second bilayer.

Both experimentally measured and calculated spectra show an abrupt blue shift of the spectral response, indicating a weaker hydrogen bond environment, consistent with a transition to a state with more liquid-like character. These theoretical results explain the experimentally observed sudden change in the SFG spectra, and thus the interfacial water organization, around 257 K in terms of a transition from one to two molten bilayers. Because of the discreteness of the ice lattice, it is reasonable that the variation of the QLL with increasing temperature occurs in a discrete manner, i.e., in a bilayer-by-bilayer fashion. "Patches" of molten bilayers in large crystalline samples would be thermodynamically unfavorable, as there would be a penalty from the liquid–solid interface. Hence, we attribute the observed change to the transition of the QLL thickness from one to two bilayers. Interestingly, such a transition seems to have been observed as well by photoelectron spectroscopy experiments; the inferred thickness seems to suddenly change between 248 K and 258 K but was not investigated in more detail (10). Layer by layer melting has been found for other systems (37, 38). In particular, for crystals with directional bonds, tendencies for layering are pronounced (39). However, for most of these systems, blocked surface melting, i.e., a finite thickness of the QLL up to the bulk melting point, has been observed (37). In contrast, for ice with its tetrahedral H-bonded structure, at low temperature, we observe a sharp transition from one to two layers, i.e., an indication for stepwise melting, whereas, for temperatures close the melting point, a divergent increase of the layer thickness has been reported (10, 12–14, 16). Therefore, water seems to be one of the few cases showing stepwise melting at low temperature and diverging melting at higher temperature.

From our experimental SFG data alone, we cannot strictly exclude that the observed transition represents the onset of surface

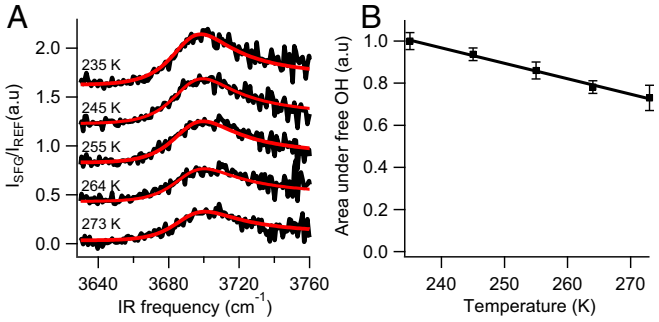

Fig. 3. SFG spectra of the basal face in the free OH region. (*A*) SFG spectra from 3,630 cm^{-1} to 3,760 cm^{-1} at different temperatures. Data are offset for clarity; the solid lines are to guide the eyes. Note that, due to different acquisition time and laser power, the intensity cannot be compared with the intensity in Fig. 2*A*. (*B*) Spectra area of the free OH vibration vs. temperature.

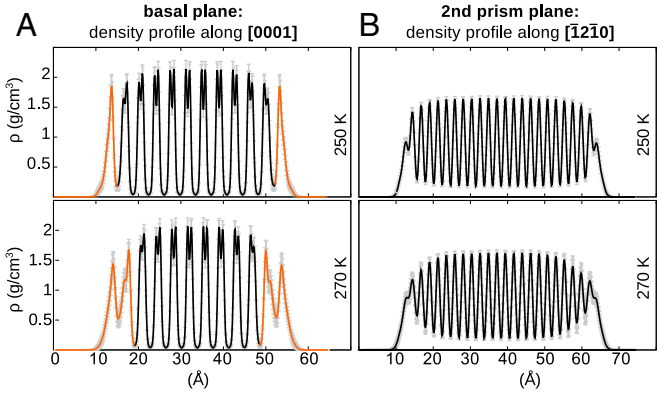

Fig. 4. Density profiles. Density profiles obtained with the TIP4P/Ice model for (*A*) the basal and (*B*) the secondary prism plane of ice Ih, illustrating the bilayer and monolayer structure, respectively. For the basal plane at 250 K, only the outer bilayer has lost its characteristic density profile, whereas, at 270 K, the outer two bilayers are molten, as indicated by the orange color. The density profile for the secondary prism face, with equal distance between the layers, changes gradually, as indicated by a gradual transition of the envelope from a rectangular to an elliptical shape. Additional temperatures are depicted in Fig. S6. Molten (orange) vs. crystalline (black) layers are identified by (bi)layer by (bi)layer RDFs (Fig. S7).

melting, i.e., solid ice below 257 K and a QLL layer with constant or increasing thickness above 257 K, instead of the formation of one QLL layer to two QLL layers. Indeed, using gracing incidence X-ray diffraction, Dosch and coworkers (13, 16) found onset temperatures of 259.5 K (−13.5 °C) for the basal and 260.5 K (−12.5 °C) for nonbasal surfaces. Although the transition temperatures are slightly lower in our experiments, we find the same trend, i.e., a lower transition temperature for the basal compared with the prism face. However, this alternative interpretation is not only at odds with the simulations presented above, it is also in seeming contradiction of the experimental observation that the response from the dangling OH groups varies modestly and continuously over our temperature window. It is unlikely that the dangling OH groups of solid ice and those of water in the QLL have the same exact vibrational frequency. Moreover, one would expect not only a frequency shift but also an intensity change, as the fast reorientational motion that is possible for the free dangling OH groups (40) in the QLL is expected to significantly affect the vibrational response. Indeed, previous SFG results have witnessed a change in the order parameter of the dangling OH at 200 K, which is a measure of the disorder of the surface. Below 200 K, the order parameter is constant, whereas, above 200 K, the order parameter decreases with increasing temperature (20). The picture that thus emerges is that the first bilayer melts at temperatures as low as 200 K, and that surface melting proceeds from 257 K onward. Although our results indicate that a single additional bilayer melts at this temperature, we cannot exclude a continuously increasing thickness of the QLL above this temperature.

The spectral changes associated with the transition provide information about the change in the local environment of the water molecules. Comparing the spectral response at 235 K and that at 269 K, the former has a strong contribution from ice and likely a (small) contribution from the very thin QLL present already at 235 K. The high temperature spectrum has a larger contribution of the QLL, as this spectrum originates from a state with at least two molten bilayers, and contains a smaller contribution from the ice, as the ice signal decreases in amplitude with increasing temperature. The analysis of the temperature-dependent spectra reveals that the contribution of the 235 K spectrum goes down with increasing temperature as the tetrahedral hydrogen bond structure in ice gets more disordered with increasing temperature. As the number of water layers abruptly increases at 257 K, so does the central frequency of the spectral response (Figs. 2*B* and 5*B*). The shift to higher frequency of the 269 K spectrum compared with the 235 K spectrum indicates a weakening of the hydrogen bonds for the QLL layer compared with ice. For the free OH groups, the small gradual decrease observed in both the experimental and the calculated SFG spectra could indicate a small decrease in ordered free OH groups with increasing temperature and/or an increased rotational mobility of these groups.

The stepwise change in the SFG spectrum observed for the basal face is also observed for the secondary prism face, albeit with a smaller, less pronounced frequency change in the experimental spectra (Fig. 2*B*). Also, the transition in the contribution of the 269 K spectrum after fitting the data with a linear combination of the spectra at low and high temperatures is less pronounced (Fig. S5). A possible explanation for the smaller step may be that, for the secondary prism face, single layers of ice melt, as the layer–layer interaction does not give rise to bilayer behavior for this crystal cut.

Although it is clear that as the temperature increases the SFG response shifts to higher frequency, a key question is about the nature of the QLL: Is it spectroscopically discernible from liquid water? To answer this question, we compare, in Fig. 7, the normalized SFG spectra from supercooled water and ice, both recorded at 269 K. The supercooled water spectrum looks similar to water spectra above zero degrees, indicating little difference between the surfaces of supercooled water and water at ambient temperatures, in contrast to bulk measurements for more strongly supercooled water (41).

For the ice surface at 269 K, we expect to probe both the ice–QLL and QLL–water interfaces. The response differs substantially from that of the supercooled water–air interface. The two spectra look very similar around 3,200 cm^{-1} (the small difference at low frequency can at least in part be attributed to a higher relative contribution of NR signal at 269 K than at 243 K), but, between 3,300 cm^{-1} and 3,500 cm^{-1}, the relative intensity in the ice spectrum is much lower than that of the supercooled water. The ice spectrum at 269 K resembles more the ice spectrum at 243 K than the supercooled water spectrum. This comparison could suggest that, at 269 K, the ice–QLL interface still significantly contributes to the observed SFG spectrum and/or that the QLL has a different nature than supercooled water in the sense that it has stronger hydrogen bonds, possibly due to templating from the underlying crystalline ice order. However, Fig. S8 shows only

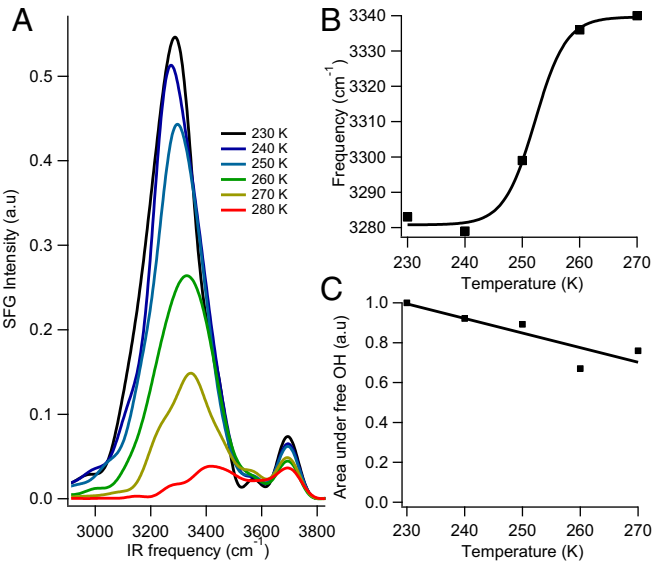

Fig. 5. Calculated SFG spectra. (*A*) Calculated *ssp* polarized SFG spectra of the basal face of ice at different temperatures. (*B*) Frequency at the maximum SFG intensity of the hydrogen-bonded peak as a function of temperature (squares) with a sigmoidal fit. (*C*) Spectral area under the free OH peak (~3,700 cm^{-1}) vs. temperature.

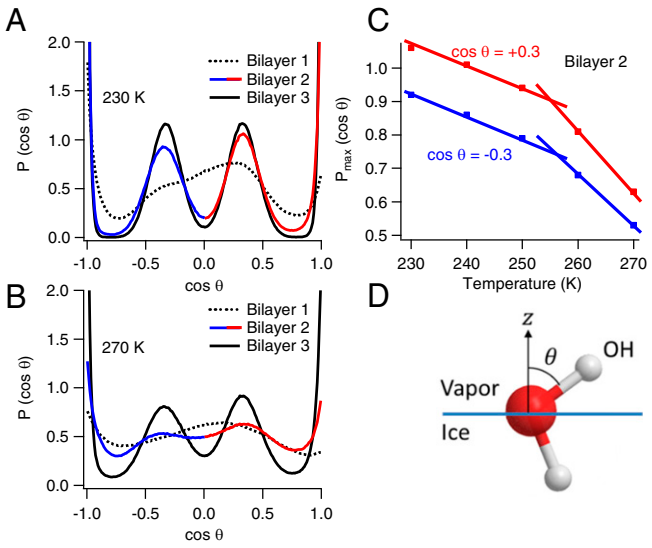

Fig. 6. O–H groups orientation. (*A* and *B*) Orientation distribution of the water OH groups for the first three bilayers at (*A*) 230 K and (*B*) 270 K. (*C*) Maxima of the orientation distribution of up- and down-pointing OH groups in the second bilayer around cos θ = 0.3 (red) and −0.3 (blue) as a function of temperature. (*D*) Definition of angle θ, so that OH groups are pointing up and down, for, respectively, positive and negative cos θ.

a slight increased ordering, i.e., tetrahedrality, for the outmost layer of ice compared with liquid water (280 K in Fig. S8) in the MD simulations.

Conclusion

Both in SFG experiments and in MD simulations, a stepwise apparent blueshift in the spectra of the ice–air interface around 257 K has been observed. This feature that indicates weakening of the hydrogen bonds marks the transition to a state in which the surface layers entail a more liquid character. The relatively small temperature variation of the dangling OH in the temperature range from 235 K to 273 K suggests that the outermost layer is not changing its nature over this temperature range. Therefore, we conclude that, already at 235 K, a QLL is present on ice. This quasi-liquid water layer suddenly increases its thickness around 257 K in a discrete bilayer-by-bilayer manner. A comparison of the SFG response of ice at 270 K with that of supercooled water at the same temperature indicates that the QLL is more similar to ice than to supercooled liquid water: The QLL seems to have stronger hydrogen bonds than liquid water. This information is crucial for understanding both the surface chemistry on ice under near-freezing conditions (42–44) and the melting mechanism of the ice surface, which has important geophysical implications on the macroscopic scale of our planet, such as for glacier sliding (45).

Materials and Methods

Sample Preparation. As described in more detail in *Supporting Information*, single crystalline ice Ih was grown by seed extraction from a melt (29). A single crystalline seed is used as the starting point. The crystallinity of the sample was checked with a Rigsby stage (46). Subsequently, a sample with the desired surface face (i.e., basal or secondary prism) was cut with a band saw. The orientation of the sample was confirmed using Formvar etching (47) (2% m/v) and X-ray diffraction. Before SFG measurements, oriented samples were mounted in a homemade stainless steel sample holder and flattened with a modified microtome (using disposable diamond-coated blades; C.L Sturkey, Inc.) and a clean oxidized silicon wafer. Finally, the ice sample was annealed for at least 24 h in the closed sample holder at 253 K. All of the components that were in contact with ice (i.e., band saw blade and sample cell) were cleaned with acetone and ethanol and rinsed with deionized water. In addition, silicon wafers were heated at 500 °C.

The secondary prism ice samples were oriented with the *c* axis perpendicular to the plane formed by the incident laser light and the surface normal.

SFG Setup. A Ti:sapphire regenerative amplifier (Spitfire Ace; Spectra-Physics) generates laser pulses (5 mJ at 1 kHz) centered at 800 nm with a pulse duration of 40 fs; 1 mJ of the laser output is used to pump a commercial optical parametric amplifier (TOPAS-C; Spectra-Physics). The signal and idler output were difference-frequency mixed in a silver gallium disulfide ($AgGaS_2$) crystal to generate IR pulses around 3,000 cm^{-1} and 3,600 cm^{-1} (FMWH ~250 cm^{-1}) with pulse energies at the sample of 3 μJ and 1.5 μJ, respectively. The visible probe pulse (20 μJ, FWHM 20 cm^{-1}) was obtained by frequency narrowing 1 mJ of the laser output in an etalon (SLS Optics Ltd.). The incident angles of the IR and visible beams were 40° and 51°, respectively, with respect to the surface normal.

The ice spectra were collected under *ssp* polarization and normalized to a nonresonant signal from a gold-coated (~100 nm) silicon wafer. The 380-μm-thick gold-coated silicon wafer (0.25 cm^2) was placed on top of the ice surface outside the ice area probed with SFG. In the SFG experiments, the infrared laser pulse is resonant with the molecular vibration. To avoid surface melting during experiments in the hydrogen-bonded region, the repetition rate of the infrared was reduced to 250 Hz and the sample was moved with a pivot crank mechanism at a speed of 2.8 cm/s. In this way, every laser shot was at a new position; after ~3 s, the laser returned back to the same position. Typical acquisition times are around 10 min. The supercooled water and ice spectra at 269 K in Fig. 7 are acquired for 60 min and 140 min, respectively.

As the cleanliness of the ice alters the premelting QLL thickness (48), we carefully checked that the ice surface is free from organic impurities by measuring the CH stretch SFG signal. No detectable C–H contamination was present, as shown in Fig. S4. The reproducibility of the spectra between different samples manifests that the surface was also free from nonorganic contaminants.

MD Simulations. MD simulations were performed to compute the density profiles, RDFs, and tetrahedral order parameter of ice surfaces. To examine whether different MD setups affect the density profiles of ice, we performed two MD simulations with different cell size and different number of water molecules. The TIP4P/Ice model (36) was used for water molecules. The details of the MD simulations are given in *Supporting Information*. The obtained 40-ns MD trajectories were used to compute density profiles, radial distributions function, and tetrahedral order parameter.

Subsequently, we computed SFG spectra of ice. Because the OH stretch vibrational mode cannot be described by the fixed-body water model and the dipole moment of water cannot be described accurately with a nonpolarizable model, the fixed-body and nonpolarizable TIP4P/Ice water model is not applicable to the SFG spectra calculation. Instead, we used the polarizable and flexible-body charge response kernel (CRK) water model (49). The simulation details can be found in *Supporting Information*. The obtained total ~1-ns MD trajectory with the CRK water model were used to compute the SFG spectra of ice.

Calculation of SFG Spectra. The *ssp* polarized SFG intensity, $I_{SFG}(\omega)$, is given by the square of the *xxz* component of the second-order nonlinear susceptibility $\chi_{xxz}^{(2)}(\omega)$, where the *xy* plane is parallel to the surface and the *z* axis forms the normal to the surface. The $\chi^{(2)}(\omega)$ is composed of a vibrationally resonant part $\chi^{(2),R}(\omega)$ and a nonresonant part $\chi^{(2),NR}$

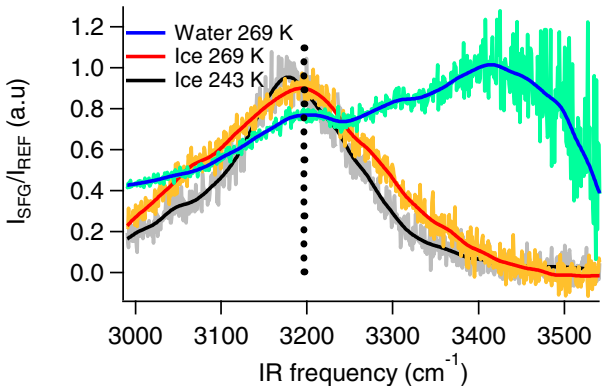

Fig. 7. SFG spectra of ice and supercooled water. Normalized SFG spectra of supercooled liquid water (green/blue) and ice, both at 269 K (orange/red), and ice at 243 K (gray/black). The lines are to guide the eye.

$$\chi^{(2)}(\omega) = \chi^{(2),R}(\omega) + \chi^{(2),NR}. \quad [1]$$

The $\chi_{xxz}{}^{(2),R}(\omega)$ can be accessed by calculating the time correlation function of the *z* component of the dipole moment (M_z) and the *xx* component of the polarizability (A_{xx}) as (50)

$$\chi^{R}_{xxz}(\omega_{IR}) = \frac{i\omega_{IR}}{k_B T}\int_0^{\tau_c} dt \exp(i\omega_{IR}t)\langle A_{xx}(t) M_z(0)\rangle, \quad [2]$$

where ω_{IR} is the IR frequency, k_B is the Boltzmann constant, and T is the temperature; τ_c was set to 1.2 ps. The polarizability and dipole moment were calculated with the local field correction using the CRK model (49). To suppress the noise of the time correlation function, Eq. **2**, due to the limited length of the MD trajectories, we used the damping treatment on the distant intermolecular correlation (51), with a cutoff distance of 5.6 Å O–O distance. To be consistent with experimental data, $\chi^{(2),NR} = -0.15$ was used for constructing the $I_{SFG}(\omega)$ spectra in Fig. 5.

ACKNOWLEDGMENTS. We thank Joan Fitzpatrick, Frederik Fleißner, Rémi Khatib, Hailong Li, Xiao Ling, Sapun Parekh, and Marialore Sulpizi for discussions and Florian Gericke for excellent technical support. The Max Planck Graduate Center is acknowledged for funding.

1. Faraday M (1859) On regelation, and on the conservation of force. *Philos Mag* 17(113):162–169.
2. Rosenberg R (2005) Why is ice slippery? *Phys Today* 58(12):50–55.
3. Dash JG, Rempel AW, Wettlaufer J (2006) The physics of premelted ice and its geophysical consequences. *Rev Mod Phys* 78(3):695–741.
4. Lipowsky R (1982) Critical surface phenomena at first-order bulk transitions. *Phys Rev Lett* 49(21):1575–1578.
5. Henson BF, Voss LF, Wilson KR, Robinson JM (2005) Thermodynamic model of quasi-siliquid formation on H_2O ice: Comparison with experiment. *J Chem Phys* 123(14): 144707.
6. Bishop CL, et al. (2009) On thin ice: Surface order and disorder during pre-melting. *Faraday Discuss* 141:277–292, and discussion (2009) 141:309–346.
7. Conde MM, Vega C, Patrykiejew A (2008) The thickness of a liquid layer on the free surface of ice as obtained from computer simulation. *J Chem Phys* 129(1):014702.
8. Kroes G-J (1992) Surface melting of the (0001) face of TIP4P ice. *Surf Sci* 275(3): 365–382.
9. Asakawa H, Sazaki G, Nagashima K, Nakatsubo S, Furukawa Y (2015) Prism and other high-index faces of ice crystals exhibit two types of quasi-liquid layers. *Cryst Growth Des* 15(7):3339–3344.
10. Bluhm H, Ogletree DF, Fadley CS, Hussain Z, Salmeron M (2002) The premelting of ice studied with photoelectron spectroscopy. *J Phys Condens Matter* 14(8):L227–L233.
11. Butt H-J, Döppenschmidt A, Hüttl G, Müller E, Vinogradova OI (2000) Analysis of plastic deformation in atomic force microscopy : Application to ice. *J Chem Phys* 113(3):1194–1203.
12. Döppenschmidt A, Butt H-J (2000) Measuring the thickness of the liquid-like layer on ice surfaces with atomic force microscopy. *Langmuir* 16(16):6709–6714.
13. Dosch H, Lied A, Bilgram J (1995) Glancing-angle X-ray scattering studies of the premelting of ice surfaces. *Surf Sci* 327(1-2):145–164.
14. Furukawa Y, Yamamoto M, Kuroda T (1987) Ellipsometric study of the transition layer on the surface of an ice crystal. *J Cryst Growth* 82(4):665–677.
15. Goertz MP, Zhu X-Y, Houston JE (2009) Exploring the liquid-like layer on the ice surface. *Langmuir* 25(12):6905–6908.
16. Lied A, Dosch H, Bilgram JH (1994) Surface melting of ice Ih single crystals revealed by glancing angle x-ray scattering. *Phys Rev Lett* 72(22):3554–3557.
17. Sazaki G, Zepeda S, Nakatsubo S, Yokomine M, Furukawa Y (2012) Quasi-liquid layers on ice crystal surfaces are made up of two different phases. *Proc Natl Acad Sci USA* 109(4):1052–1055.
18. Li Y, Somorjai GA (2007) Surface premelting of ice. *J Phys Chem C* 111(27):9631–9637.
19. Shen YR (1989) Surface properties probed by second-harmonic and sum-frequency generation. *Nature* 337(6207):519–525.
20. Wei X, Miranda PB, Shen YR (2001) Surface vibrational spectroscopic study of surface melting of ice. *Phys Rev Lett* 86(8):1554–1557.
21. Wei X, Miranda PB, Zhang C, Shen YR (2002) Sum-frequency spectroscopic studies of ice interfaces. *Phys Rev B* 66(8):085401.
22. Barnett IL, Groenzin H, Shultz MJ (2011) Hydrogen bonding in the hexagonal ice surface. *J Phys Chem A* 115(23):6039–6045.
23. Bisson PJ, Shultz MJ (2013) Hydrogen bonding in the prism face of ice I(h) via sum frequency vibrational spectroscopy. *J Phys Chem A* 117(29):6116–6125.
24. Groenzin H, Li I, Buch V, Shultz MJ (2007) The single-crystal, basal face of ice I(h) investigated with sum frequency generation. *J Chem Phys* 127(21):214502.
25. Groenzin H, Li I, Shultz MJ, Jane M (2008) Sum-frequency generation: Polarization surface spectroscopy analysis of the vibrational surface modes on the basal face of ice I(h). *J Chem Phys* 128(21):214510.
26. Rossend R, Møller KB, Hynes JT (2002) Hydrogen bond dynamics in water and ultrafast infrared spectroscopy. *J Phys Chem A* 106(50):11993–11996.
27. Lawrence CP, Skinner JL (2003) Vibrational spectroscopy of HOD in liquid D_2O. III. Spectral diffusion, and hydrogen-bonding and rotational dynamics. *J Chem Phys* 118(264):264–272.
28. Bernal JD, Fowler RH (1933) A theory of water and ionic solution, with particular reference to hydrogen and hydroxyl ions. *J Chem Phys* 1(8):515–548.
29. Roos DVDS (1975) Rapid production of single crystals of ice. *J Glaciol* 14(71):325–328.
30. Higashi A, Oguro M, Fukuda A (1968) Growth of ice single crystals from the melt, with special reference to dislocation structure. *J Cryst Growth* 3(4):728–732.
31. Czochralski J (1918) A new method for the measurement of the crystallization rate of metals. *Z Phys Chem* 92:219–221.
32. Rigsby GP (1951) Crystal fabric studies on Emmons Glacier Mount Rainier, Washington. *J Geol* 59(6):590–598.
33. Shultz MJ, Bisson P, Groenzin H, Li I (2010) Multiplexed polarization spectroscopy: Measuring surface hyperpolarizability orientation. *J Chem Phys* 133(5):054702.
34. Ishiyama T, Morita A (2014) A direct evidence of vibrationally delocalized response at ice surface. *J Chem Phys* 141(18):18C503.
35. Ishiyama T, Takahashi H, Morita A (2012) Origin of vibrational spectroscopic response at ice surface. *J Phys Chem Lett* 3(20):3001–3006.
36. Abascal JLF, Sanz E, García Fernández R, Vega C (2005) A potential model for the study of ices and amorphous water: TIP4P/Ice. *J Chem Phys* 122(23):234511.
37. van der Veen JF (1999) Melting and freezing at surfaces. *Surf Sci* 433-435:1–11.
38. Mei QS, Lu K (2007) Melting and superheating of crystalline solids: From bulk to nanocrystals. *Prog Mater Sci* 52(8):1175–1262.
39. van der Gon AWD, Gay JM, Frenken JWM, van der Veen JF (1991) Order-disorder transitions at the Ge (111) surface. *Surf Sci* 241(3):335–345.
40. Wei X, Shen YR (2001) Motional effect in surface sum-frequency vibrational spectroscopy. *Phys Rev Lett* 86(21):4799–4802.
41. Nilsson A, Pettersson LGM (2015) The structural origin of anomalous properties of liquid water. *Nat Commun* 6(8998):8998.
42. Abbatt JPD (2003) Interactions of atmospheric trace gases with ice surfaces: Adsorption and reaction. *Chem Rev* 103(12):4783–4800.
43. Bartels-Rausch T, et al. (2014) A review of air–ice chemical and physical interactions (AICI): Liquids, quasi-liquids, and solids in snow. *Atmos Chem Phys* 14(3):1587–1633.
44. Shepherd TD, Koc MA, Molinero V (2012) The Quasi-liquid layer of ice under conditions of methane clathrate formation. *J Phys Chem C* 116(22):12172–12180.
45. Cuffey KM, Conway H, Hallet B, Gades AM, Raymond CF (1999) Interfacial water in polar glaciers and glacier sliding at −17°C. *Geophys Res Lett* 26(6):751–754.
46. Langway CCJ (1958) *Ice Fabrics and the Universal Stage* (US Army Snow Ice Permafrost Res Establ, Wilmette, IL), Tech Rep 62.
47. Roos DVDS (1966) Two-dimensional grain growth in ice. *J Glaciol* 6(45):411–420.
48. Wettlaufer JS (1999) Impurity effects in the premelting of ice. *Phys Rev Lett* 82(12): 2516–2519.
49. Ishiyama T, Morita A (2009) Analysis of anisotropic local field in sum frequency generation spectroscopy with the charge response kernel water model. *J Chem Phys* 131(24):244714.
50. Morita A, Hynes JT (2002) A theoretical analysis of the sum frequency generation spectrum of the water surface. II. Time-dependent approach. *J Phys Chem B* 106(3): 673–685.
51. Nagata Y, Mukamel S (2010) Vibrational sum-frequency generation spectroscopy at the water/lipid interface: Molecular dynamics simulation study. *J Am Chem Soc* 132(18):6434–6442.
52. Shultz MJ, Brumberg A, Bisson PJ, Shultz R (2015) Producing desired ice faces. *Proc Natl Acad Sci USA* 112(45):E6096–E6100.
53. Higuchi K (1958) The erching of ice crystals. *Acta Metall* 6(10):636–642.
54. Lohmeier M, Vlieg E (1993) Angle calculations for a six-circle surface X-ray diffractometer. *J Appl Cryst* 26(5):706–716.
55. Buch V, Sandler P, Sadlej J (1998) Simulations of H_2O solid, liquid, and clusters, with an emphasis on ferroelectric ordering transition in hexagonal ice. *J Phys Chem B* 102(44): 8641–8653.
56. Parrinello M, Rahman A (1981) Polymorphic transitions in single crystals: A new molecular dynamics method. *J Appl Phys* 52(12):7182–7190.
57. Hoover WG (1985) Canonical dynamics: Equilibrium phase-space distributions. *Phys Rev A Gen Phys* 31(3):1695–1697.
58. Nosé S (1984) A unified formulation of the constant temperature molecular dynamics methods. *J Chem Phys* 81(1):511–519.
59. Hess B, Kutzner C, van der Spoel D, Lindahl E (2008) GROMACS 4: Algorithms for highly efficient, load-balanced, and scalable molecular simulation. *J Chem Theory Comput* 4(3):435–447.
60. Bussi G, Donadio D, Parrinello M (2007) Canonical sampling through velocity rescaling. *J Chem Phys* 126(1):014101.
61. Todorov IT, Smith W, Dove MT (2006) DL_POLY_3: New dimensions in molecular dynamics simulations via massive parallelism. *J Mater Chem* 16(20):1911–1918.
62. Berendsen HJC, Postma JPM, van Gunsteren WF, DiNola A, Haak JR (1984) Molecular dynamics with coupling to an external bath Molecular dynamics with coupling to an external bath. *J Chem Phys* 81(8):3684–3690.
63. Jochum M, Andrienko D, Kremer K, Peter C (2012) Structure-based coarse-graining in liquid slabs. *J Chem Phys* 137(6):064102.
64. Fortes AD, et al. (2004) No evidence for large-scale proton ordering in Antarctic ice from powder neutron diffraction. *J Chem Phys* 120(24):11376–11379.